Research Article Vol. 33, No. 24 / 1 Dec 2025 / Optics Express 51499
Optics EXPRESS

Modeling method for concentric ring resonators with dispersion engineering

MEHEDI HASAN,[1] SEUNGYUP BAEK,[2] AYRTON BERNUSSI,[1] AND SANGSIK KIM[2,*]

[1]Department of Electrical and Computer Engineering and Nano Tech Center, Texas Tech University, Lubbock, Texas 79409-3102, USA
[2]School of Electrical Engineering, Korea Advanced Institute of Science and Technology, Daejeon 34141, Republic of Korea
*sangsik.kim@kaist.ac.kr

Abstract: We introduce a geometry-guided design method in concentric ring resonators for dispersion engineering. Using eigenmode simulations of a single ring, we construct a two-dimensional round-trip optical path length (OPL) map that systematically identifies phase-matched geometries without exhaustive parameter sweeps. The OPL map finds feasible ring and gap combinations for efficient coupling, also revealing the design limits. With this approach, we design a 50 nm-thick Si_3N_4 concentric ring resonator that achieves anomalous dispersion in a weakly-guided mode—a regime that typically exhibits normal dispersion in single-ring configurations. Lugiato–Lefever equation (LLE) simulations confirm that this dispersion-engineered concentric ring can support a bright soliton in a weakly guided mode, overcoming the dispersion limit due to a weak confinement. The proposed modeling method is generalized and readily extendable to a wide range of material platforms and wavelength regimes, providing a powerful tool for diverse integrated nonlinear photonic applications.

1. Introduction

Microresonators, especially in the form of ring resonators, are fundamental components of integrated photonics, enabling optical frequency combs, wavelength division multiplexer (WDM) filters, high-speed modulators, and sensors [1–9]. These applications rely on precise control of dispersion, which governs the phase-matching for wave-mixing, channel bandwidths in WDM filters, signal linearity in high-speed modulators, and sensitivity of optical sensors. The precise control of dispersion is especially critical for microcomb generation, as it directly governs the microcomb initiation, bandwidth, shape, and stability [10–13].

Conventional dispersion engineering relies on parametric sweeps of single-ring cross-section [14–18], which often require thick films to achieve high confinement for anomalous dispersion. However, such a thick silicon nitride film tends to crack and poses fabrication challenges [19–21]. Moreover, dispersion issues become more challenging in visible and ultraviolet regions, where most materials intrinsically exhibit strong normal dispersion. To address these limitations, mode coupling or avoided mode crossing has been widely explored to introduce localized but strong anomalous dispersion. This mechanism has been linked to microcomb generation across various high-Q microresonator platforms [22–24], yet it often arises from accidental mode interactions with limited engineering capability. Here, concentric microresonators provide an additional degree of freedom for dispersion engineering through controlled modal interaction between the inner and outer rings. This modal coupling leads to the formation of symmetric and anti-symmetric supermodes, whose dispersion profiles can be reshaped via avoided mode crossings. Consequently, concentric ring geometries can provide more versatile dispersion profiles, enabling near-zero or anomalous dispersion even in spectral regimes typically dominated by strong material dispersion.

#577296 https://doi.org/10.1364/OE.577296
Journal © 2025 Received 28 Aug 2025; revised 17 Nov 2025; accepted 17 Nov 2025; published 26 Nov 2025

Optics EXPRESS

Recent studies have confirmed the feasibility of this modal coupling approach, clearly showing how concentric resonator configurations can induce avoided mode crossings and reshape the dispersion profiles [25–30]. Nevertheless, most prior works still rely on heuristic parameter sweeps and extensive numerical simulations, which are computationally expensive and limit broader applicability. Therefore, developing a systematic and broadly applicable modeling method capable of accurately predicting coupling conditions without exhaustive computational searches is still highly needed.

Such a systematic modeling method is especially beneficial for addressing dispersion challenges associated with weakly-guided modes [31–34]. Recently, ultra-high-Q resonators utilizing weakly-guided modes have been developed on ultrathin Si_3N_4 films (<100 nm) cladded by thick (>6 μm) low-loss oxides [32,35]. Due to their low index contrast and weak confinement, these modes naturally exhibit normal dispersion, limiting their potential. For example, in Kerr microcomb generation, anomalous dispersion is required for bright soliton formation, while normal dispersion yields dark solitons. Thus, with a weakly-guided mode, a dark soliton generation has been demonstrated first [36], while bright solitons in this platform have only recently been demonstrated with laterally coupled racetrack resonators [37,38].

In this paper, we present a generalized, geometry-guided modeling method for dispersion engineering in concentric ring resonators, utilizing optical path length (OPL) maps from eigenmode analysis of single-ring resonators. Using this method, we systematically identify geometric parameters, including outer and inner ring dimensions and the gap between them, and provide design guidelines for optimizing modal coupling for dispersion control. As a proof-of-concept demonstration, we apply our method to design a 50 nm-thick Si_3N_4 resonator, successfully achieving anomalous dispersion in a weakly-guided mode, a regime particularly challenging due to weak optical confinement that leads to normal dispersion. Lugiato–Lefever equation (LLE) simulations further confirm that our design supports the single bright soliton formation in a weakly-guided resonator. Given its solely geometric basis, our modeling approach is broadly applicable across diverse material platforms and wavelength ranges, offering an efficient tool for versatile dispersion engineering.

2. Modeling method for a concentric ring resonator

2.1. Concept and schematics of a concentric ring resonator

Figure 1(a) illustrates the proposed concentric ring resonator scheme. Two rings with different radii (R_{out} and R_{in}) and widths (w_{out} and w_{in}) are positioned in the same plane, sharing a common center. The ring radius is defined as the distance from the origin to the outer boundary of the ring. The widths of each ring are typically $w_{out}<w_{in}$ to match the round-trip phase accumulations between outer and inner rings. This condition is necessary because the inner ring has a shorter physical circumference compared to the outer ring, thus requiring a higher effective refractive index to maintain equal phase around the ring.

Figure 1(b) shows the cross-sectional view of the concentric ring resonator, comprising Si_3N_4 resonator core embedded within an upper and lower silicon dioxide (SiO_2) claddings. Here, we choose Si_3N_4 as an example for its low loss and broadband transparency window, but the proposed configuration can be readily applied to other platforms.

When two individual rings with matched round-trip phase accumulation are brought into proximity, their evanescent fields overlap, leading to mode coupling. This interaction hybridizes modes and gives rise to new collective eigenstates, called supermodes, that span both rings. These supermodes are typically classified as symmetric or antisymmetric modes based on their electric-field profiles. Figure 1(c) visualizes these distinct field distributions, showing normalized radial electric field component Re(E_r). While the symmetric mode exhibits an in-phase field distribution across both rings, the antisymmetric mode shows a distinct phase reversal between them. The formation of supermodes transforms the system from two individually perturbed

Optics EXPRESS

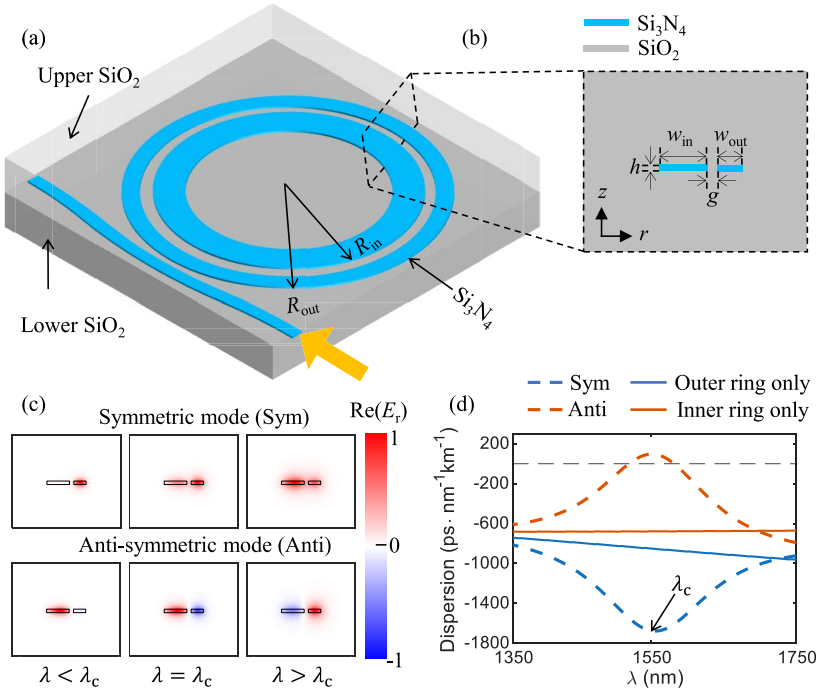

Fig. 1. Device schematics and dispersion engineering in concentric ring resonators. (a) Schematic of the concentric ring resonator having outer and inner radii R_{out} and R_{in}, respectively. The Si_3N_4 core is embedded between upper and lower SiO_2 claddings. (b) Cross-sectional view illustrating the geometrical parameters: the inner and outer ring widths w_{in} and w_{out}, thickness h, and gap g. (c) Normalized radial electric field [Re(E_r)] distributions of symmetric (Sym) and anti-symmetric (Anti) supermodes at the coupling wavelength λ_c and the detuned wavelengths. (d) Dispersion curves for the coupled supermodes (Sym: blue dashed, Anti: orange dashed) compared with those of uncoupled modes in the outer (blue solid) and inner (orange solid) rings. Strong dispersion deviations occur at the λ_c. Geometric parameters are R_{out} = 100 μm, R_{in} = 98.1 μm, w_{in} = 2.6 μm, w_{out} = 1.4 μm, h = 0.3 μm, and g = 0.5 μm.

resonators into a coupled system described by collective eigenstates. Thus, resonant frequencies and dispersion properties are no longer limited to individual rings but instead are determined by their mutual interactions. This coupling introduces an additional degree of freedom, enabling dispersion control that surpasses the capabilities of conventional single-ring geometries alone.

2.2. *Analysis of a mode coupling and dispersion engineering*

Phase matching is essential for efficient mode coupling and formation of hybridized supermodes. This has been pointed out in several studies related to avoided mode crossings in concentric resonator structures [26,28]. In this section, we clarify how phase matching leads to mode coupling and enables dispersion engineering using the coupled-mode theory represented in a cylindrical coordinate [39].

For wave propagation along the azimuthal direction ($0 \le \theta \le 2\pi$), the coupled-mode equations for two asymmetric waveguides can be expressed as follows:

$$\frac{da_1}{R_1 d\theta} = i\beta_1 a_1 + i\kappa_{12} a_2, \tag{1a}$$

Optics EXPRESS

$$\frac{da_2}{R_2 d\theta} = i\beta_2 a_2 + i\kappa_{21} a_1, \tag{1b}$$

where a_1 and a_2 represent the modal amplitudes in each waveguide, β_1 and β_2 are the propagation constants of the uncoupled mode, κ_{12} and κ_{21} are the coupling coefficients between modes in each ring, and R_1 and R_2 are the radii of the outer and inner rings, respectively. Here, the propagation constants β and coupling coefficients κ are calculated using bent waveguide eigenmodes, reflecting bending effects compared to straight waveguides. Under lossless and reciprocal conditions, the coupling coefficients satisfy $\kappa_{12} = -\kappa_{21}^* \equiv \kappa$.

To simplify our analysis, we introduce the azimuthal propagation constant $\beta_{\theta i} = \beta_i R_i$ for each ring $i = 1, 2$. Note that β_i and R_i are related, thus defining one inherently determines the other one, but their product remains constant. Thus, in a cylindrical coordinate, the azimuthal propagation constant β_θ is an intuitive parameter to assess phase accumulation around the ring; this is often referred to as the OPL matching condition in literature [26,40]. The coupled-mode equations can be rewritten as:

$$\frac{da_1}{d\theta} = i\beta_{\theta 1} a_1 + iR_1 \kappa_{12} a_2, \tag{2}$$

$$\frac{da_2}{d\theta} = i\beta_{\theta 2} a_2 + iR_2 \kappa_{21} a_1. \tag{3}$$

Assuming supermode solutions of the form $a_1(\theta) = A_1 e^{i\gamma\theta}$ and $a_2(\theta) = A_2 e^{i\gamma\theta}$, where γ is the eigenvalue of the coupled system representing the azimuthal propagation constant of supermodes (i.e., $\gamma = \beta_{\theta\pm} = \beta_\pm R_\pm$). Solving the eigenvalue for γ, we obtain:

$$\gamma = \beta_{\theta\pm} = \frac{\beta_{\theta 1} + \beta_{\theta 2}}{2} \pm \sqrt{\left(\frac{\beta_{\theta 1} - \beta_{\theta 2}}{2}\right)^2 + R_1 R_2 |\kappa|^2}. \tag{4}$$

The term under the square root includes both phase mismatch and the coupling strength $|\kappa|$, determining the degree of splitting between symmetric and anti-symmetric modes and consequently controlling their dispersions. This term can be defined as the dispersion splitting term $\Delta(\omega)$, given by:

$$\Delta(\omega) = \sqrt{\left(\frac{\beta_1 R_1 - \beta_2 R_2}{2}\right)^2 + R_1 R_2 |\kappa|^2}. \tag{5}$$

The dispersion parameter $D_\pm(\omega)$ for the coupled symmetric (+) and anti-symmetric (-) modes can thus be expressed as [41]:

$$D_\pm(\omega) = -\frac{\omega^2}{2\pi c}\frac{d^2\beta_\pm}{d\omega^2} = D_0 \mp \frac{\omega^2}{2\pi c R_\pm}\frac{d^2\Delta}{d\omega^2} \tag{6}$$

where D_0 is the average intrinsic dispersion of the individual uncoupled single rings.

Mode coupling in a concentric ring resonator occurs when the round-trip phase accumulation (or OPLs) around the rings closely match. Since one round-trip OPL of a resonator is defined as OPL $= 2\pi R_{\text{eff}} n_{\text{eff}}$, where n_{eff} and R_{eff} are the effective refractive index and radius of the ring, respectively, the OPL matching condition at a given wavelength implies $\beta_1 R_1 = \beta_2 R_2 = \beta_0 R_0$

Optics EXPRESS

(i.e., azimuthal propagation constant matching). Accounting this, Eq. (4) simplifies to:

$$\gamma = \beta_0 R_0 \pm |\kappa|\sqrt{R_1 R_2} \tag{7}$$

Assuming the effective radii of the coupled modes are approximately equal (i.e., $R_\pm = \sqrt{R_1 R_2} = R_0$), the dispersion parameter in Eq. (6) at coupling frequency ω_c can be simplified to:

$$D_\pm(\omega)\big|_{\omega=\omega_c} = D_0 \mp \frac{\omega^2}{2\pi c}\frac{d^2|\kappa(\omega)|}{d\omega^2} \tag{8}$$

Note that the dispersion of the supermodes $D_\pm$ is directly governed by the second derivative of the coupling strength $|\kappa|$ with respect to angular frequency ω. Typically, the coupling strength $|\kappa|$ exhibits a convex frequency dependence, implying a positive second derivative:

$$\frac{d^2|\kappa|}{d\omega^2} > 0.$$

Consequently, with appropriate coupling, the dispersion of the anti-symmetric mode can reach anomalous dispersion ($D_- > 0$), even when the intrinsic dispersion D_0 is in the normal dispersion regime ($D_0 < 0$). This is shown in Fig. 1(d), which plots the dispersion parameter $D_\pm$ for both supermodes as a function of wavelength. Near the OPL-matched coupling wavelength λ_c, strong modal hybridization causes an avoided mode crossing; the modes repel and diverge rather than crossing, leading to a sharp reshaping of their dispersion profiles. This enables a localized transition from normal to anomalous dispersion within a certain spectral window. Slight detuning from OPL matching ($\beta_1 R_1 \approx \beta_2 R_2$) still causes noticeable dispersion shifts, as shown by the curvature around the peak coupling region in Fig. 1(d). By tailoring geometric parameters such as the gap size and ring widths, the position and bandwidth of the anomalous dispersion region can be engineered. Thus, this method provides a powerful approach to dispersion engineering beyond the conventional waveguide cross-section optimization method alone.

2.3. Resonant mode coupling in a concentric ring resonator

Now, the hybridized guided modes form new basis sets for resonant modes. These hybridized supermodes must be carefully designed for avoided mode crossing, considering the resonance condition. A single-ring resonance condition is $m\lambda_m = 2\pi R_{\text{eff}} n_{\text{eff}}$ ($\equiv$ OPL), where m is the azimuthal mode number and λ_m is the resonant wavelength. Achieving hybridized modes requires careful matching of the round-trip OPLs between the inner and outer rings, given by: $2\pi R_{\text{out}} n_{\text{out}} = 2\pi R_{\text{in}} n_{\text{in}}$, where subscripts out and in denote the outer and inner rings, respectively. Combining the resonant conditions with the mode coupling requirement, the coupling condition can be expressed as: $m\lambda_m^{\text{out}} = n\lambda_n^{\text{in}}$, where m and n represent azimuthal mode numbers of the outer and inner rings, respectively. Thus, designing ring geometries that satisfy this condition at a target wavelength results in resonant mode coupling. Figure 2 shows this resonant mode coupling matching, demonstrating how individual ring geometries can be designed at a target wavelength. Figures 2(a) and 2(b) show the cross-sections of the individual outer and inner Si_3N_4 rings with their geometric parameters. Each single ring supports a distinct resonant mode due to its unique geometry and corresponding modal index. Figure 2(c) shows the coupled concentric ring structure with a small gap, enabling their optical field overlap to support a coupling. Figure 2(d) plots numerically simulated round-trip OPLs ($m\lambda_m$) of each ring as a function of wavelength λ. Since simulations return discrete eigenfrequencies for each integer m, the data points are discrete. However, we plot with continuous line graphs to explicitly show the coupling and mode splitting. Two solid lines represent the round-trip OPLs of uncoupled outer (blue) and inner (orange) rings, while two dashed lines are those of coupled symmetric (blue) and anti-symmetric (orange) modes. The zoomed-in inset clearly shows the intersection between the OPLs of the inner and outer rings,

Optics EXPRESS

corresponding to the OPL matching condition. Near this matching wavelength, the two coupled modes split, resulting in modal dispersion due to avoided mode crossing. The dispersion plots shown in Fig. 1(d) are directly derived from this OPL data in Fig. 2(d), illustrating the capability of dispersion engineering via mode coupling. Overall, OPL calculations enable precise targeting of coupling wavelengths, offering systematic modeling capability for concentric ring resonators.

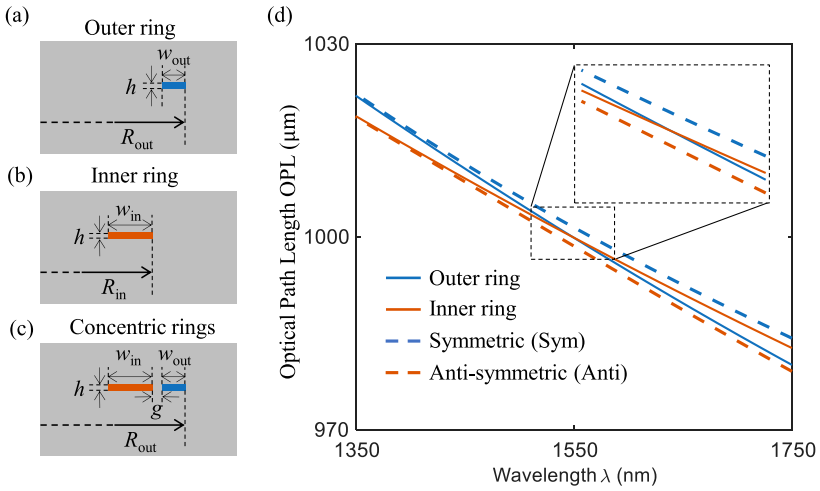

Fig. 2. Round-trip optical path length (OPL) matching using eigenmode analysis. (a)-(c) Cross-sectional geometries of (a) outer, (b) inner, and (c) concentric rings. (d) Simulated round-trip OPLs versus wavelength: outer ring (solid blue), inner ring (solid orange), symmetric (dashed blue), and anti-symmetric (dashed orange) modes. The intersection of the solid curves indicates phase-matching near 1550 nm, corresponding to the onset of coupling. Geometric parameters are the same as in Fig. 1.

2.4. Design methodology for a concentric ring resonator

To systematically design mode coupling at a desired wavelength λ_c, we propose a geometric modeling method based on single-ring eigenmode simulations. First, eigenmode simulations of a single ring are conducted over a chosen geometric parameter space, spanning ranges of radius $R \in [R_1, R_2]$ and waveguide width $w \in [w_1, w_2]$. From each simulation, we extract (m, λ_m) set and form the modal product OPL = $m\lambda_m$. Compiling the results, we can construct a two-dimensional OPL map, with contours representing configurations of the identical OPLs.

Figure 3 shows the simulated OPL map of a single-ring SiN resonator (h = 300 nm-thick) as a function of R = 95 – 105 μm and w = 0.6 – 3.5 μm. Different colors represent different OPLs, allowing rapid identification of resonator geometries of the same OPLs. To determine the mode coupling pair, we begin by selecting the outer ring parameters. Here, we chose radius R_{out} = 100 μm and width w_{out} = 1.4 μm, represented as point **A** on the map. Next, we trace the contour line corresponding to the OPL at point **A** (purple dashed line). To define the inner ring geometry, we shift horizontally to the left by a distance equal to the difference between the outer and inner ring radii, i.e., $w_{out} + g$, identifying point **B**. In other words, the inner ring radius is defined as $R_{in} = R_{out} - (w_{out} + g)$. Here, we chose w_{out} = 1.4 μm and g = 0.5 μm, resulting in R_{in} = 98.1 μm. From point **B**, a perpendicular line is drawn toward the contour line, determining the intersection point **C**. This intersection identifies the required inner ring width, here w_{in} = 2.6 μm. The ring parameters used in Figs. 1 and 2 were obtained using this parameter extraction procedure. This method simplifies the design process for concentric rings, eliminating

Optics EXPRESS

the need for computationally intensive simulations of the fully coupled structure. The entire design procedure is summarized in Table 1.

This OPL map provides a direct visualization of the single-ring phase accumulation, where the contour line indicates phase matching ($\beta_1 R_1 \approx \beta_2 R_2$) and thus predicts the geometry at which the avoided mode crossing occurs. The resulting dispersion reshaping in the coupled structure is then governed by the coupling strength κ, which depends on the modal overlap and gap separation. Accordingly, the OPL contours highlight where coupling and dispersion perturbations arise across geometry space, while κ determines how strongly they manifest in the coupled dispersion $D_{\pm}(\omega)$. Moreover, it defines the feasible geometric limits, including the maximum gap that determines the degree of dispersion detuning. Once the outer ring geometry is fixed on the OPL map (point **A**), the corresponding inner ring radius follows $R_{\text{in}} = R_{\text{out}} - (w_{\text{out}} + g)$. Due to the steep slope of contour lines near the lower edge of the map, the inner ring radius cannot be arbitrarily small. The minimum feasible inner ring radius occurs where the OPL contour intersects the vertical axis, limiting the maximum allowable gap at a given outer ring geometry. Consequently, adjusting outer ring parameters directly influences the maximum gap for coupling. From the OPL contour map in Fig. 3, it can be observed that decreasing the outer ring width (moving upward along the contour) generally increases the maximum allowable gap. Similarly, increasing the outer ring radius (moving rightward along the contour) also expands the feasible gap range. These trends provide a qualitative guide for the initial selection of concentric ring geometries; the outer ring width can be minimized to maximize design flexibility, while being sufficiently large to maintain a high confinement for a higher Q. Likewise, a larger outer ring radius increases the allowable gap range but results in increased cavity volume, a trade-off that must be considered. The tolerance analysis presented in Appendix A further quantifies how such geometric trade-offs manifest in real fabrication scenarios, highlighting the relative impact of width and gap variations on the resulting dispersion response.

Table 1. Step-by-step geometry-guided design procedure for concentric ring resonator

Step 1	**Prepare input parameters**
	• Target coupling wavelength λ_c
	• Radius range ($R \in [R_1, R_2]$) and width range ($w \in [w_1, w_2]$)
	• Gap between rings (g)
Step 2	**Construct a 2D OPL map plot**
	• Run FEM eigenmode simulations of a single ring at the target wavelength λ_c for each combination of $R \in [R_1, R_2]$ and $w \in [w_1, w_2]$
	• Plot a 2D OPL $= m\lambda_m$ contour map as functions of (R, w) (Fig. 3)
Step 3	**Find $(R_{\text{out}}, w_{\text{out}})$ and $(R_{\text{in}}, w_{\text{in}})$ set using the OPL map**
	• Select a point $\mathbf{A} = (R_{\text{out}}, w_{\text{out}})$ representing the outer ring
	• Trace the contour line passing through point **A**
	• Determine the inner ring radius $R_{\text{in}} = R_{\text{out}} - w_{\text{out}} - g$ (point **B**)
	• Determine the inner ring width w_{in}, following the contour line with R_{in} (point $\mathbf{C} = (R_{\text{in}}, w_{\text{in}})$)
Step 4	**Output parameters**
	Coordinates of $\mathbf{A} = (R_{\text{out}}, w_{\text{out}})$ and $\mathbf{C} = (R_{\text{in}}, w_{\text{in}})$ define the concentric ring resonator that supports mode coupling at λ_c.

One may also reverse the process, i.e., starting from point **C** to find the corresponding point **A**, which might make the process easier. This geometry-guided approach can also be extended to design multiple coupled-ring resonators [42], enabling broader exploration of dispersion

Optics EXPRESS

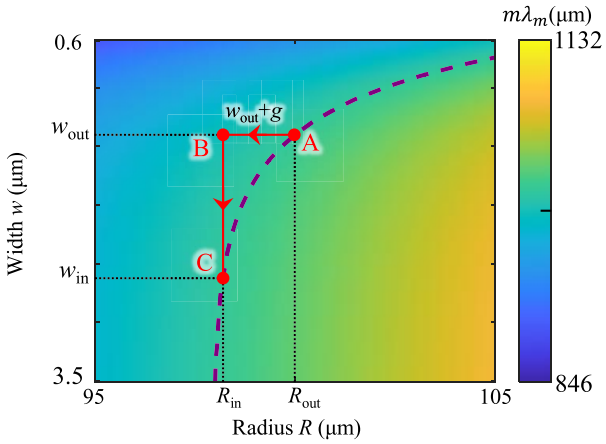

Fig. 3. 2D OPL map for parameter extraction of a concentric ring resonator. The map is constructed from the OPL of a single ring as functions of ring radius $R \in [95, 105]$ μm and width $w \in [0.6, 3.5]$ μm. The design procedure begins by selecting an outer ring point **A** (R_{out}, w_{out}) and tracing its corresponding contour (purple dashed line). The inner ring radius is defined by $R_{in} = R_{out} - (w_{out} + g)$ (point **B**), from which a vertical projection intersects the contour at point **C**, yielding the inner ring geometry (R_{in}, w_{in}). This procedure provides a systematic method to identify phase-matched inner and outer rings at the target wavelength λ_c.

engineering strategies beyond a single mode coupling alone. Appendix B further demonstrates the use of the OPL-based design across different materials platforms and wavelength ranges.

3. Concentric ring resonators with a weakly-guided mode

3.1. Achieving anomalous dispersion with a weakly-guided mode

The modeling method introduced in Sec. 2 is broadly applicable to various material platforms and spectral regimes. Among other platforms, this method is particularly effective for resonators supporting a weakly-guided mode. Recently, an ultrathin Si_3N_4 resonator, characterized by core thicknesses below 100 nm and thick low-loss oxide claddings, has emerged as a prominent platform, achieving extremely low propagation losses (<0.06 dB/m) and ultra-high quality factors (Q>400 million) [32,35]. Due to its low optical confinement, such resonators typically require a large bending radius, resulting in a smaller free spectral range (FSR, on the order of tens of GHz) compared to thick high confinement Si_3N_4 resonators (typically, on the order of hundreds to thousands of GHz). Consequently, the ultra-high-Q and relatively narrow FSRs make the weakly-guided resonators attractive for narrow linewidth laser sources [36,43–45] and high-precision frequency comb applications [36,38,46], while making the platform compatible with CMOS technology.

However, weakly-guided resonators inherently exhibit strong normal dispersion due to their low optical confinement, limiting their conventional single-ring microcomb formation to dark solitons [36,47]. Recent approaches using laterally coupled racetrack resonators have demonstrated effective dispersion engineering, achieving anomalous dispersion and enabling bright soliton generation [37,38]. However, these approaches often produce soliton pulse pairs, limiting independent control of comb parameters such as repetition rate and pulse phase.

In this section, we show that the concentric ring resonator design, guided by the design method introduced in Sec. 2, provides an alternative to overcome these limitations. By precisely

Optics EXPRESS

controlling geometric parameters and carefully engineering mode coupling between inner and outer rings, anomalous dispersion can be directly realized even in resonators characterized by strong normal dispersion. We apply our design method to a 50 nm-thick Si_3N_4 resonator, achieving anomalous dispersion at an FSR of approximately 10 GHz. Using the dispersion profile obtained through our concentric ring design, we numerically solve the LLE and demonstrate stable bright soliton microcomb generation at ≈ 10 GHz repetition rates, highlighting the effectiveness of our approach in a weakly-guided resonator.

Figure 4 demonstrates the proposed concentric ring resonator design approach with a low-loss weakly-guided mode platform. Figure 4(a) shows the OPL map plot as a function of the ring radius and waveguide width for the 50 nm-thick Si_3N_4 scheme (inset: scheme). Since the mode sizes are relatively large, the bending radius is on the order of millimeters (~3 mm) and the waveguide width is in several micrometers (~2-6 μm). For this design, the outer ring radius is chosen to be 3 mm (with the ring width of 2.45 μm), which corresponds to a FSR of approximately 10.6 GHz. Then, using the method in Sec. 2, we found the inner ring parameters as R_{in} = 2.99 mm and w_{in} = 5.71 μm to achieve the mode coupling near 1550 nm. Figure 4(b) shows the electric field profiles of the coupled concentric ring, showing the coupled symmetric and anti-symmetric modes with a low optical confinement. By sweeping the azimuthal mode numbers, we can obtain the corresponding resonant frequencies, from which the FSRs are extracted as shown in Fig. 4(c). Near the coupling wavelength, the FSRs are exchanged between the symmetric (blue circles) and anti-symmetric (orange circles) modes, while away from the coupling region, both modes asymptotically approach the FSRs of the uncoupled outer and inner rings. Note that the slopes of the FSR curves ($\frac{\delta FSR}{\delta \lambda}$) are positive for all modes, indicating normal dispersion, except for the antisymmetric mode near the coupling wavelength. The negative slope in antisymmetric mode suggests the appearance of anomalous dispersion. This is clearly shown in the extracted dispersion plot in Fig. 4(d), confirming that our mode coupling approach is also effective for the weakly-guided platform as well.

3.2. *Bright soliton generation in a weakly-guided concentric resonator*

The anomalous dispersion profile obtained in Sec. 3.1 can be used to form a bright Kerr soliton in a weakly-guided mode. Previously, a dark soliton was initially demonstrated with a weakly-guided ring due to its normal dispersion profile caused by weak confinement [36]. While dark solitons are useful for power-efficient operation, bright solitons are desired for applications requiring short pulses with high peak power, such as optical frequency synthesis [48], dual-comb spectroscopy [49], and low-jitter microwave photonics [50]. Here, we numerically show that bright-soliton generation is possible in the weakly-guided structure shown in Fig. 4.

We used the LLE to simulate bright soliton generation [51]. The dispersion profile of the anti-symmetric mode in Fig. 4 was used for this LLE simulation. Due to low confinement, the effective modal volume V_{eff} is about two orders of magnitude larger than that of a typical high confinement silicon nitride resonator [52]. Since the parametric oscillation threshold scales as $\sim V_{\text{eff}}/Q^2$, such an increase in modal volume would require a higher threshold power for soliton formation. However, this is compensated by the platform's ultra-high intrinsic Q factor, which is also enhanced by approximately two orders of magnitude. In our LLE simulation, an intrinsic Q factor of 150 million [36] and critical coupling were assumed. This enabled bright soliton generation with a threshold power of 2.6 mW when pumping the anomalous dispersion mode near 1550 nm. Figure 5(a) shows the simulated spectrum, which has the characteristic hyperbolic secant shape of a bright soliton. The soliton step as a function of pump wavelength detuning is also shown in Fig. 5(b). The inset shows the intracavity power distribution over the resonator polar angle θ, confirming a single localized bright pulse circulating in the cavity. Generating bright solitons in a weakly-guided, ultrathin Si_3N_4 platform via modal-coupling-induced anomalous dispersion enables low-FSR, highly coherent pulse trains. Combined with self-injection locking

Optics EXPRESS

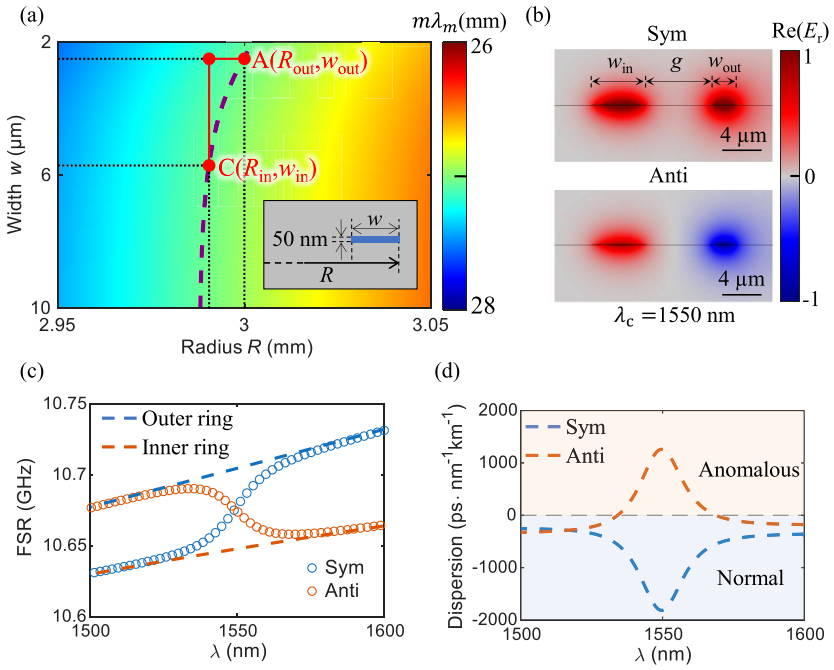

Fig. 4. Concentric ring resonator in a 50 nm-thick Si_3N_4 weakly-guided platform. (a) Optical path length (OPL) map of a single 50 nm thick Si_3N_4 ring resonator as a function of radius R = 2.95 – 3.05 mm and waveguide width w = 2 – 10 μm. The inset shows the cross-section of the corresponding single Si_3N_4 ring. The points **A** and **C** denote the extracted outer and inner ring geometries, respectively: R_{out} = 3 mm, w_{out} = 2.45 μm, R_{in} = 2.99 mm, and w_{in} = 5.71 μm. The ring gap is g = 7.1 μm. (b) Electric field profiles Re(E_r) of the coupled symmetric (Sym) and anti-symmetric (Anti) supermodes. (c) Simulated free spectral ranges (FSRs) of the symmetric (blue circles) and anti-symmetric (orange circles) resonant modes. The blue and orange dashed lines represent the FSRs of the uncoupled outer and inner resonators, respectively. (d) Dispersion profiles of the symmetric (blue dash) and anti-symmetric (orange dash) mode, demonstrating the emergence of anomalous dispersion near 1550 nm.

and ultrahigh-Q, this approach could offer a promising route toward integrated microcombs with low noise and high spectral coherence. While the material system and process flow are compatible with CMOS fabrication principles, further experimental validation is required to confirm full process compatibility and device scalability for large-volume integration.

4. Conclusion

In summary, we introduced a generalized, geometry-based method for dispersion engineering in concentric microresonators. Leveraging single-ring eigenmode simulations, we constructed an OPL map that rapidly identifies phase-matched geometries without exhaustive parameter sweeps. This approach also reveals practical design limits, such as gap size and ring dimensions. We applied this method on a 50 nm-thick Si_3N_4 weakly-guided resonator, whose single-ring dispersion normally exhibits only normal dispersion. Using our modeling method, we achieved anomalous dispersion near the telecom band and numerically confirmed single bright soliton generation via LLE simulation. The modeling method is material-independent and readily applicable to various platforms and wavelength regimes.

Optics EXPRESS

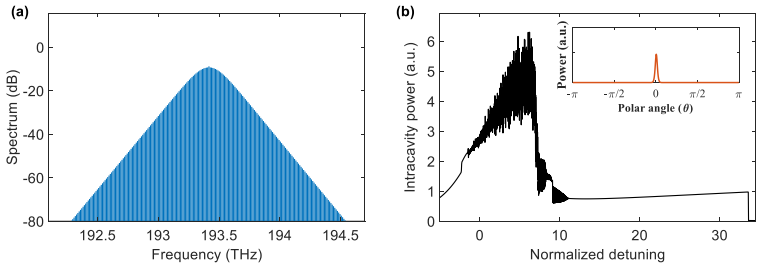

Fig. 5. Bright soliton generation in a weakly-guided concentric resonator. (a) Simulated bright soliton spectrum, exhibiting a sech^2 envelope. (b) Characteristic soliton step versus normalized detuning $\zeta_0 = \frac{2}{\kappa}(w_0 - w_p)$, where κ represents the cavity decay rate, and w_0 and w_p are the angular frequencies of the pumped resonance mode and the pump laser, respectively. Inset: the spatial profile of the intracavity pulse along the resonator's polar angle $-\pi \le \theta \le \pi$, confirming a single bright soliton. The dispersion profile from Fig. 4(a) is used, assuming an intrinsic Q of 150 million and critical coupling.

Appendix A: fabrication tolerance analysis of the 300 nm Si_3N_4 concentric microresonator

It is important to note that fabrication-induced variations can affect the designed dispersion response. Among the key structural parameters, the outer-ring width w_{out} and coupling gap g exhibit the highest sensitivity to dispersion detuning, whereas variations in the outer radius R_{out} and inner-ring width w_{in} exert relatively weaker influence.

Figure 6 presents a tolerance analysis for the 300 nm Si_3N_4 platform, incorporating realistic process deviations of ±40 nm. The figure shows the dispersion profile of the coupled antisymmetric mode of the concentric resonator described in Fig. 1, with fabrication deviations incorporated in the simulation by introducing ±5 nm steps along both ring edges, resulting in a corresponding

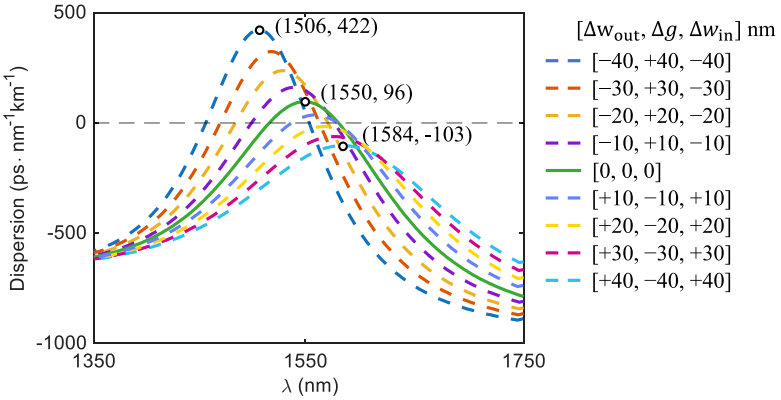

Fig. 6. Tolerance analysis for the 300 nm Si_3N_4 concentric microresonator platform. The dispersion profile of the antisymmetric mode is plotted for ring dimensions $[w_{\mathrm{out}}, g, w_{\mathrm{in}}]$ varying from [1360, 540, 2560] nm (dark-blue dashed) to [1440, 460, 2640] nm (light-blue dashed), corresponding to ±40 nm fabrication deviations. The solid green curve represents the initial design at [1400, 500, 2600] nm. The black circles denote the peak-dispersion points for the initial geometry and for ±40 nm variations in ring widths; the corresponding coupling wavelength and dispersion (in ps/nm/km) for each peak point is marked.

Optics EXPRESS

width change of ±10 nm and gap change of ∓10 nm, simultaneously. For an overall ±40 nm width tolerance, the coupling wavelength exhibits a shift of approximately ±40 nm, while the peak dispersion varies by about ∓310 ps/nm/km relative to the initial design (solid green line in Fig. 6). It should be noted that this sensitivity is specific to the given material platform and geometry; changes in material composition, film thickness, or operating wavelength would alter the degree and nature of the dispersion variation.

Appendix B: OPL-based design at different wavelength regimes and material platforms

To further demonstrate the generality of the proposed workflow, it is applied to different wavelength and material platforms. Figure 7 illustrates its extension to a 300 nm SiN platform at 1060 nm, capable of generating visible to near-infrared soliton microcombs for application in atomic spectroscopy [53], and to a 250 nm-thick AlN-on-insulator platform at 1550 nm capable of frequency comb generation [54]. The resulting OPL maps and corresponding dispersion profiles confirm that the same design method remains valid across distinct wavelength regimes and material systems, confirming the versatility of the geometry-guided approach.

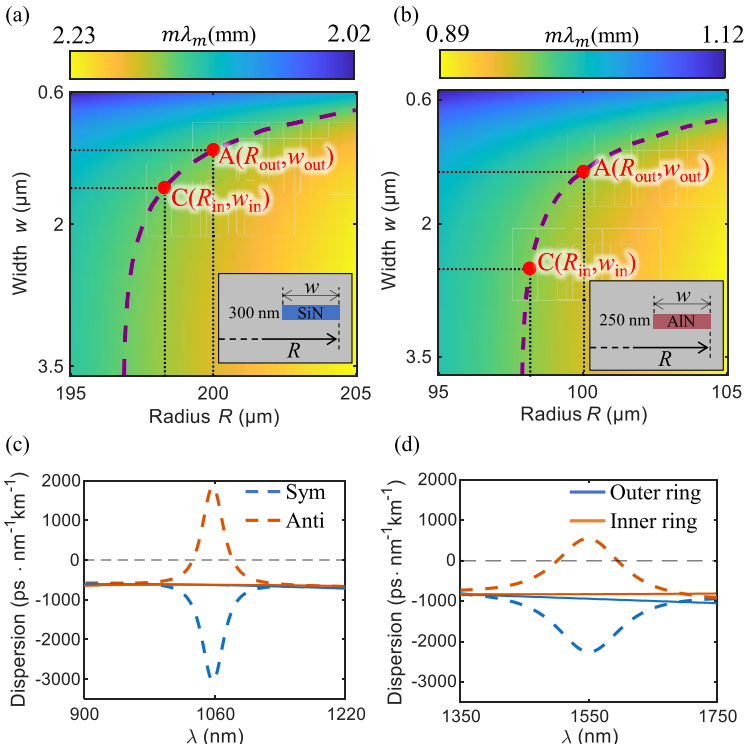

Fig. 7. Geometry-guided design method at different wavelength regimes and material platforms. 2D OPL map and concentric-ring parameter extraction for (a) 300 nm-thick SiN platform at 1060 nm wavelength and (b) 250 nm-thick AlN-on-insulator platform at 1550 nm wavelength. (c), (d) Dispersion curves for the coupled supermodes (Sym: blue dashed, Anti: orange dashed) compared with those of uncoupled modes in the outer (blue solid) and inner (orange solid) rings for the concentric-ring geometries extracted from (a) and (b), respectively. Extracted geometric parameters are: (a) R_{out} = 200 μm, R_{in} = 198.29 μm, w_{in} = 1.61 μm, w_{out} = 1.21 μm, h = 0.3 μm, and g = 0.5 μm; and (b) R_{out} = 100 μm, R_{in} = 98.14 μm, w_{in} = 2.65 μm, w_{out} = 1.41 μm, h = 0.25 μm, and g = 0.45 μm.

Optics EXPRESS

Funding. National Science Foundation (2144568); Institute for Information and Communications Technology Promotion (RS-2023-00223497); BK21 FOUR (Connected AI Education & Research Program for Industry and Society Innovation, KAIST EE, No. 4120200113769).

Acknowledgments. This work was supported by Samsung Advanced Institute of Technology.

Disclosures. The authors declare no conflicts of interest.

Data availability. The data underlying the results presented in this paper are not publicly available at this time but may be obtained from the authors upon reasonable request.

References

1. T. J. Kippenberg, R. Holzwarth, and S. A. Diddams, "Microresonator-based optical frequency combs," Science **332**(6029), 555–559 (2011).
2. Y. Xuan, Y. Liu, L. T. Varghese, *et al.*, "High-Q silicon nitride microresonators exhibiting low-power frequency comb initiation," Optica **3**(11), 1171–1180 (2016).
3. L. Chang, S. Liu, and J. E. Bowers, "Integrated optical frequency comb technologies," Nat. Photonics **16**(2), 95–108 (2022).
4. W.-C. Hsu, N. Nujhat, B. Kupp, *et al.*, "On-chip wavelength division multiplexing filters using extremely efficient gate-driven silicon microring resonator array," Sci. Rep. **13**(1), 5269 (2023).
5. J. Hong, F. Qiu, X. Cheng, *et al.*, "A high-speed electro-optic triple-microring resonator modulator," Sci. Rep. **7**(1), 4682 (2017).
6. J. Wang, K. Liu, M. W. Harrington, *et al.*, "Silicon nitride stress-optic microresonator modulator for optical control applications," Opt. Express **30**(18), 31816–31827 (2022).
7. M. R. Bryan, J. N. Butt, J. Bucukovski, *et al.*, "Biosensing with silicon nitride microring resonators integrated with an on-chip filter bank spectrometer," ACS Sens. **8**(2), 739–747 (2023).
8. S. Z. Ahmed, M. Hasan, K. Kim, *et al.*, "Zero-crosstalk silicon photonic refractive index sensor with subwavelength gratings," Nano Convergence **11**(1), 39 (2024).
9. Z. Yao, K. Wu, B. X. Tan, *et al.*, "Integrated silicon photonic microresonators: emerging technologies," IEEE J. Sel. Top. Quantum Electron. **24**(6), 5900324 (2018).
10. Y. K. Chembo, I. S. Grudinin, and N. Yu, "Spatiotemporal dynamics of Kerr-Raman optical frequency combs," Phys. Rev. A **92**(4), 043818 (2015).
11. T. Herr, M. L. Gorodetsky, and T. J. Kippenberg, *Dissipative Kerr Solitons in Optical Microresonators* (John Wiley & Sons, Ltd, 2016), Chap. 6, pp. 129–162.
12. X. Xue, M. Qi, and A. M. Weiner, "Normal-dispersion microresonator Kerr frequency combs," Nanophotonics **5**(2), 244–262 (2016).
13. Q.-X. Ji, W. Jin, L. Wu, *et al.*, "Engineered zero-dispersion microcombs using CMOS-ready photonics," Optica **10**(2), 279–285 (2023).
14. Q. Li, T. C. Briles, D. A. Westly, *et al.*, "Stably accessing octave-spanning microresonator frequency combs in the soliton regime," Optica **4**(2), 193–203 (2017).
15. J. Chavez Boggio, D. Bodenmüller, T. Fremberg, *et al.*, "Dispersion engineered silicon nitride waveguides by geometrical and refractive-index optimization," J. Opt. Soc. Am. B **31**(11), 2846–2857 (2014).
16. Y. Zhao, X. Ji, B. Y. Kim, *et al.*, "Visible nonlinear photonics via high-order-mode dispersion engineering," Optica **7**(2), 135–141 (2020).
17. Y. Song, Y. Hu, X. Zhu, *et al.*, "Octave-spanning Kerr soliton frequency combs in dispersion-and dissipation-engineered lithium niobate microresonators," Light:Sci. Appl. **13**(1), 225 (2024).
18. H. Jung, M. Poot, and H. X. Tang, "In-resonator variation of waveguide cross-sections for dispersion control of aluminum nitride micro-rings," Opt. Express **23**(24), 30634–30640 (2015).
19. K. Luke, A. Dutt, C. B. Poitras, *et al.*, "Overcoming Si_3N_4 film stress limitations for high quality factor ring resonators," Opt. Express **21**(19), 22829–22833 (2013).
20. D. J. Moss, R. Morandotti, A. L. Gaeta, *et al.*, "New CMOS-compatible platforms based on silicon nitride and hydex for nonlinear optics," Nat. Photonics **7**(8), 597–607 (2013).
21. S. Liu, Y. Zhang, A. Hariri, *et al.*, "Fabrication of ultra-low-loss, dispersion-engineered silicon nitride photonic integrated circuits via silicon hardmask etching," ACS Photonics **12**(2), 1039–1046 (2025).
22. Y. Liu, Y. Xuan, X. Xue, *et al.*, "Investigation of mode coupling in normal-dispersion silicon nitride microresonators for Kerr frequency comb generation," Optica **1**(3), 137–144 (2014).
23. G. Lin and T. Sun, "Mode crossing induced soliton frequency comb generation in high-Q yttria-stabilized zirconia crystalline optical microresonators," Photonics Res. **10**(3), 731–739 (2022).
24. S. Ramelow, A. Farsi, S. Clemmen, *et al.*, "Strong polarization mode coupling in microresonators," Opt. Lett. **39**(17), 5134–5137 (2014).
25. M. Soltani, A. Matsko, and L. Maleki, "Enabling arbitrary wavelength frequency combs on chip," Laser Photonics Rev. **10**(1), 158–162 (2016).
26. S. Kim, K. Han, C. Wang, *et al.*, "Dispersion engineering and frequency comb generation in thin silicon nitride concentric microresonators," Nat. Commun. **8**(1), 372 (2017).

Optics EXPRESS

27. G. Moille, Q. Li, S. Kim, *et al.*, "Phased-locked two-color single soliton microcombs in dispersion-engineered Si_3N_4 resonators," Opt. Lett. **43**(12), 2772–2775 (2018).
28. Y. Zhang, K. Zhong, X. Zhou, *et al.*, "Broadband high-Q multimode silicon concentric racetrack resonators for widely tunable Raman lasers," Nat. Commun. **13**(1), 3534 (2022).
29. Z. Wang, L. Luo, D. Xia, *et al.*, "Engineered octave frequency comb in integrated chalcogenide dual-ring microresonators," Front. Photon. **4**, 1066993 (2023).
30. H. Cheng, G. Lin, D. Xia, *et al.*, "Multi-octave two-color soliton frequency comb in integrated chalcogenide microresonators," Front. Optoelectron. **17**(1), 36 (2024).
31. D. T. Spencer, J. F. Bauters, M. J. Heck, *et al.*, "Integrated waveguide coupled Si_3N_4 resonators in the ultrahigh-Q regime," Optica **1**(3), 153–157 (2014).
32. M. W. Puckett, K. Liu, N. Chauhan, *et al.*, "422 million intrinsic quality factor planar integrated all-waveguide resonator with sub-MHz linewidth," Nat. Commun. **12**(1), 934 (2021).
33. N. Chauhan, J. Wang, D. Bose, *et al.*, "Ultra-low loss visible light waveguides for integrated atomic, molecular, and quantum photonics," Opt. Express **30**(5), 6960–6969 (2022).
34. D. Bose, M. W. Harrington, A. Isichenko, *et al.*, "Anneal-free ultra-low loss silicon nitride integrated photonics," Light:Sci. Appl. **13**(1), 156 (2024).
35. K. Liu, N. Jin, H. Cheng, *et al.*, "Ultralow 0.034 dB/m loss wafer-scale integrated photonics realizing 720 million Q and 380 μw threshold Brillouin lasing," Opt. Lett. **47**(7), 1855–1858 (2022).
36. W. Jin, Q.-F. Yang, L. Chang, *et al.*, "Hertz-linewidth semiconductor lasers using CMOS-ready ultra-high-Q microresonators," Nat. Photonics **15**(5), 346–353 (2021).
37. Z. Yuan, M. Gao, Y. Yu, *et al.*, "Soliton pulse pairs at multiple colours in normal dispersion microresonators," Nat. Photonics **17**(11), 977–983 (2023).
38. P. Liu, Q.-X. Ji, J.-Y. Liu, *et al.*, "Near-visible integrated soliton microcombs with detectable repetition rates," Nat. Commun. **16**(1), 4780 (2025).
39. H. A. Haus, *Waves and Fields in Optoelectronics* (Prentice-Hall, 1984).
40. H. Ji, Z. Geng, W. Cheng, *et al.*, "High-power two-color Kerr frequency comb generation on the gallium phosphide-on-insulator platform at SWIR and MIR spectra," J. Opt. Soc. Am. B **40**(8), 1976–1985 (2023).
41. M. B. Mia, N. Jaidye, and S. Kim, "Extremely high dispersions in heterogeneously coupled waveguides," Opt. Express **27**(8), 10426–10437 (2019).
42. S. Fatema, M. B. Mia, and S. Kim, "Multiple mode couplings in a waveguide array for broadband near-zero dispersion and supercontinuum generation," J. Lightwave Technol. **39**(1), 216–222 (2021).
43. S. Gundavarapu, G. M. Brodnik, M. Puckett, *et al.*, "Sub-hertz fundamental linewidth photonic integrated Brillouin laser," Nat. Photonics **13**(1), 60–67 (2019).
44. K. Liu, K. D. Nelson, R. O. Behunin, *et al.*, "Large mode volume integrated Brillouin lasers for scalable ultra-low linewidth and high power," Nat. Commun. **16**(1), 6419 (2025).
45. K. Liu, N. Chauhan, J. Wang, *et al.*, "36 Hz integral linewidth laser based on a photonic integrated 4.0 m coil resonator," Optica **9**(7), 770–775 (2022).
46. Z. Sun, Y. Li, B. Bai, *et al.*, "Silicon nitride-based Kerr frequency combs and applications in metrology," Adv. Photonics **4**(06), 064001 (2022).
47. B. Shen, L. Chang, J. Liu, *et al.*, "Integrated turnkey soliton microcombs," Nature **582**(7812), 365–369 (2020).
48. D. T. Spencer, T. Drake, T. C. Briles, *et al.*, "An optical-frequency synthesizer using integrated photonics," Nature **557**(7703), 81–85 (2018).
49. A. Dutt, C. Joshi, X. Ji, *et al.*, "On-chip dual-comb source for spectroscopy," Sci. Adv. **4**(3), e1701858 (2018).
50. J. Liu, E. Lucas, A. S. Raja, *et al.*, "Photonic microwave generation in the x- and k-band using integrated soliton microcombs," Nat. Photonics **14**(8), 486–491 (2020).
51. L. A. Lugiato, F. Prati, M. L. Gorodetsky, *et al.*, "From the Lugiato–Lefever equation to microresonator-based soliton Kerr frequency combs," Philos. Trans. R. Soc., A **376**(2135), 20180113 (2018).
52. H. Guo, M. Karpov, E. Lucas, *et al.*, "Universal dynamics and deterministic switching of dissipative Kerr solitons in optical microresonators," Nat. Phys. **13**(1), 94–102 (2017).
53. S.-P. Yu, T. C. Briles, G. T. Moille, *et al.*, "Tuning Kerr-soliton frequency combs to atomic resonances," Phys. Rev. Appl. **11**(4), 044017 (2019).
54. H. Jung, C. Xiong, K. Y. Fong, *et al.*, "Optical frequency comb generation from aluminum nitride microring resonator," Opt. Lett. **38**(15), 2810–2813 (2013).